Hydrophobically Modified Silica-Coated

Gold Nanorods for Generating Nonlinear

Photoacoustic Signals

Evan N. Mueller, ^{1,‡} Maju Kuriakose, ^{2,‡} Saheli Ganguly, ¹ Ke Ma, ¹ Marco A. Inzunza-Ibarra, ² Todd W. Murray, ^{2,*} Jennifer N. Cha, ^{1,3,*} and Andrew P. Goodwin ^{1,3,*}

¹Department of Chemical and Biological Engineering, ²Department of Mechanical Engineering, ³Materials Science and Engineering Program, University of Colorado, 596 UCB, Boulder, Colorado 80309, United States.

KEYWORDS Photoacoustic imaging, gold nanorod, mesoporous silica, cavitation, nonlinear optics.

In this work, we report that gold nanorods coated with hydrophobically-modified mesoporous silica shells not only enhance photoacoustic (PA) signal over unmodified mesoporous silica coated gold nanorods, but that the relationship between PA amplitude and input laser fluence is strongly nonlinear. Mesoporous silica shells of ~14 nm thickness and with ~3 nm pores were grown on gold nanorods showing near infrared absorption. The silica was rendered hydrophobic with addition of dodecyltrichlorosilane, then re-suspended in aqueous media with a lipid monolayer. Analysis of the PA signal revealed not only an enhancement of PA signal compared to mesoporous silica coated gold nanorods at lower laser fluences, but also a nonlinear relationship between PA signal and laser fluence. We attribute each effect to the entrapment of solvent vapor in the

mesopores: the vapor has both a larger expansion coefficient and thermal resistance than silica that enhances conversion to acoustic energy, and the hydrophobic porous surface is able to promote phase transition at the surface, leading to a nonlinear PA response even at fluences as low as 5 mJ cm⁻². At 21 mJ cm⁻², the highest laser fluence tested, the PA enhancement was >12-fold over mesoporous silica coated gold nanorods.

Photoacoustic (PA) imaging has garnered widespread interest in recent years due to its ability to image structural and functional properties of biological tissues and organs at depth inside of scattering media. Unlike purely optical techniques such as optical coherence tomography, PA imaging does not rely on ballistic light to create an image and rather exploits diffuse photons to excite acoustic waves that travel back to the specimen surface with minimal scattering. 1–8 Advantages in imaging are derived from the ability of optical waves to capture wavelength-dependent optical information and transfer this information to a detector using acoustic waves. In general, a PA response occurs when a molecule or object absorbs directly incident light (typically of a pulsed laser with a few nanoseconds pulse width or modulated continuous wave laser) and converts this energy to acoustic waves through transient thermal expansion. 9 In biomedical imaging applications, these acoustic waves are detected outside the body and processed to produce an image of the subsurface absorption profile, or used in sensing applications. 1.2.5

While naturally-present biomolecules, like hemoglobin in blood, show endogenous PA contrast, ^{1–3,5} there has been a significant amount of recent work on developing exogeneous contrast agents to increase imaging depth and sensitivity. Such agents can be engineered to enhance the PA response through improved photoacoustic conversion efficiency and increased absorption of

excitation light at wavelengths with greater tissue penetration. ^{10–16} Numerous types of exogenous contrast agents have been developed for PA imaging, including organic dyes, organic nanoparticles, graphene, carbon nanotubes, silver nanoparticles, gold nanoparticles and others. ^{10,11,13,16–19} Of these, gold nanostructures are particularly popular because they are biocompatible, possess large absorption coefficients, and have plasmon absorption wavelengths that can be tuned into the near infrared based on the geometry of the nanostructure. ^{10–16,20–22} Gold nanostructure contrast agents have shown great potential for biomedical imaging and have also been used as guide-star targets for optical imaging in scattering tissues through wavefront shaping. ^{23–26}

There have been a number of attempts to increase the PA response from gold nanostructures, including doping the shell with iodide and wrapping the gold with graphene oxide and porphyrins.^{17–19,27,28} Most relevant to this work, Emelianov and coworkers enhanced the PA response from gold nanorods (AuNRs) by adding a silica layer that both decreased thermal resistance at the particle surface and stabilized particle shape retention,²² with reports of three-fold PA enhancement as compared to uncoated AuNRs.^{12,29–31} The mechanism of acoustic emission was reported as being caused by the thermal expansion of the silica-coated nanorod and surrounding liquid, and the enhancement was associated with an increase in thermal conductance at the Au-silica and silica-water interfaces.

In addition to thermal expansion, cavitation, or the formation and collapse of bubbles on the nanostructure surface, can increase the PA signal significantly at elevated laser fluence and thereby impart a nonlinear characteristic to the signal.³² Cavitation has been demonstrated on AuNRs through the superheating of adjacent water but at laser fluences that are quite high with respect to the maximum permissible exposure for tissue.^{33–37} In order to reduce the cavitation threshold,

Wilson *et al.* added AuNRs to a low boiling point perfluorocarbon droplet so that localized heating from the AuNRs would cause vaporization of the nanodroplet, leading to a much stronger photoacoustic response than AuNRs alone.³⁸ In another example, Dixon *et al.* showed nonlinear PA enhancement from microbubbles coated with AuNRs through vaporization of the liquid around the AuNRs.³⁹ Reports by O'Donnell and Pozzo also showed nonlinear enhancement by the combination of gold and microbubbles.⁴⁰ However, obtaining similar modes of enhancement from sub-100 nm nanoparticles has been challenging.

In this paper, we report a unique contrast agent that is designed to induce cavitation on the surface at low laser fluence and thus impart a nonlinear PA response, while also maintaining a very strong photoacoustic response in the linear regime. Previously, we showed that hydrophobically modified mesoporous silica nanoparticles facilitate acoustic cavitation by stabilizing the formation of gas pockets on the surface. 41-45 Here, gold nanorods with plasmon resonance in the NIR were coated first with silica, then covalently modified with hydrophobic alkyl chains. To impart dispersibility in aqueous solvents, the nanoparticles were resuspended with a monolayer of phospholipids (Figure 1). These hydrophobically-functionalized AuNRs showed greatly enhanced PA signal as compared to bare gold or gold coated with unfunctionalized silica, and the response transitioned from linear to non-linear at only 5 mJ cm⁻². The presence of vapor bubbles trapped in the pores first increased the PA enhancement at laser fluences below the linear to nonlinear transition, then acted as surfaces to facilitate the liquid-vapor transition of surrounding water. ⁴⁵ The nonlinear PA response can be derived from vaporization and/or bubble oscillation. ^{46,47} The particles showed good stability in biological media, and they exhibited a linear PA response with concentration. Ultimately, we envision the potential applications of these nanoparticles could include absolute measurements of nanoparticle concentration through illuminating the

nanoparticles at different fluences in the nonlinear regime, and as guide-stars in photoacoustic guided wavefront shaping where the nonlinear response could lead to improvements in focusing through scattering media.

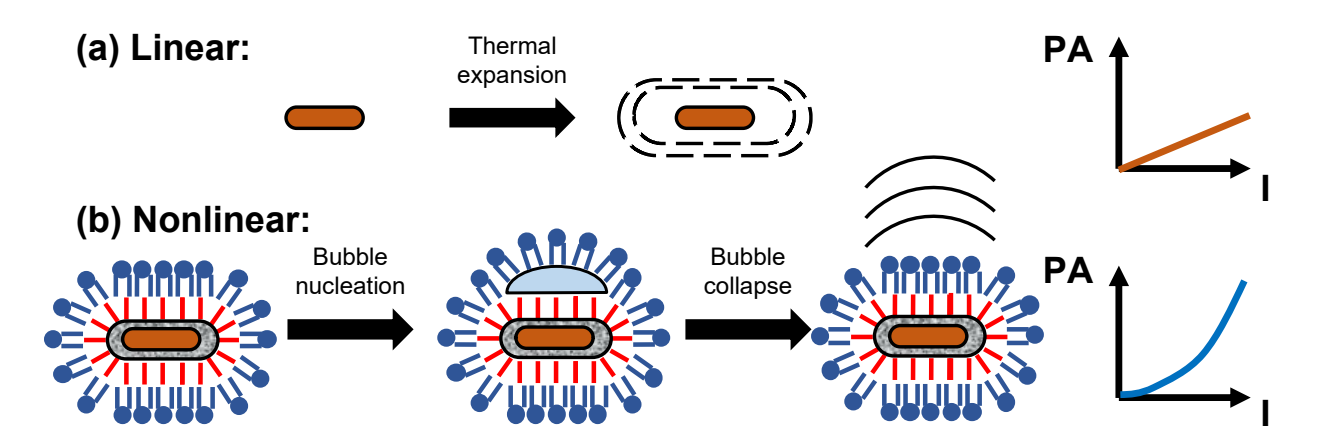


Figure 1. (a) The photoacoustic response of gold nanorods at low laser fluence is produced by the heating of the nanorods and surrounding fluid. If the physical properties of the particle and fluid are not temperature dependent, then a linear relationship between fluence and photoacoustic response is expected. (b) In surface modified silica coated nanorods, vaporization of the liquid surrounding the nanorods leads to bubble formation and a highly nonlinear photoacoustic response. Schematics are not drawn to scale.

Results and Discussion

Because previous research showed that rough, hydrophobic surfaces were optimal for stabilizing nascent bubbles, the synthesis of the nanostructures began by coating nanorods with mesoporous silica. 12,22,29,30,45,48 First, bare gold AuNRs were synthesized from gold (III) trihydride, sodium oleate, and cetrimonium bromide (CTAB) by a seed-mediated process developed by Ye *et al* (Figure 2a). 21 The aspect ratio of the rods was controlled using the pH of the growth solution. The concentration was measured by using the localized surface plasmonic resonance (LSPR) of ~765

nm and the extinction coefficient was determined from the peak wavelength (Figure 2d). ⁴⁹ Next, a modified Stöber method was used to coat the AuNRs with mesoporous silica to create MSiO2-AuNRs. ^{48,50} After diluting the AuNRs to 1 nM, the colloidal solution was basified to pH~11 and tetraethylorthosilicate (TEOS) was added to produce a silica coating of ~14 nm (Figure 2b). The UV-Vis spectra (Figure 2d) showed that coating the AuNRs with mesoporous silica resulted in a red shift of ~15 nm. At the same time, dynamic light scattering (DLS) measurements showed an increase in particle diameter from 34±15 nm to 75±30 nm, though the AuNR value is likely underestimated due to the presence of excess CTAB micelles (Table S1). ^{51,52} The zeta potential showed a large change from +24±1.7 mV to -41±1.6 mV, consistent with replacement of the CTAB stabilizing ligand with a silica shell. ⁵³

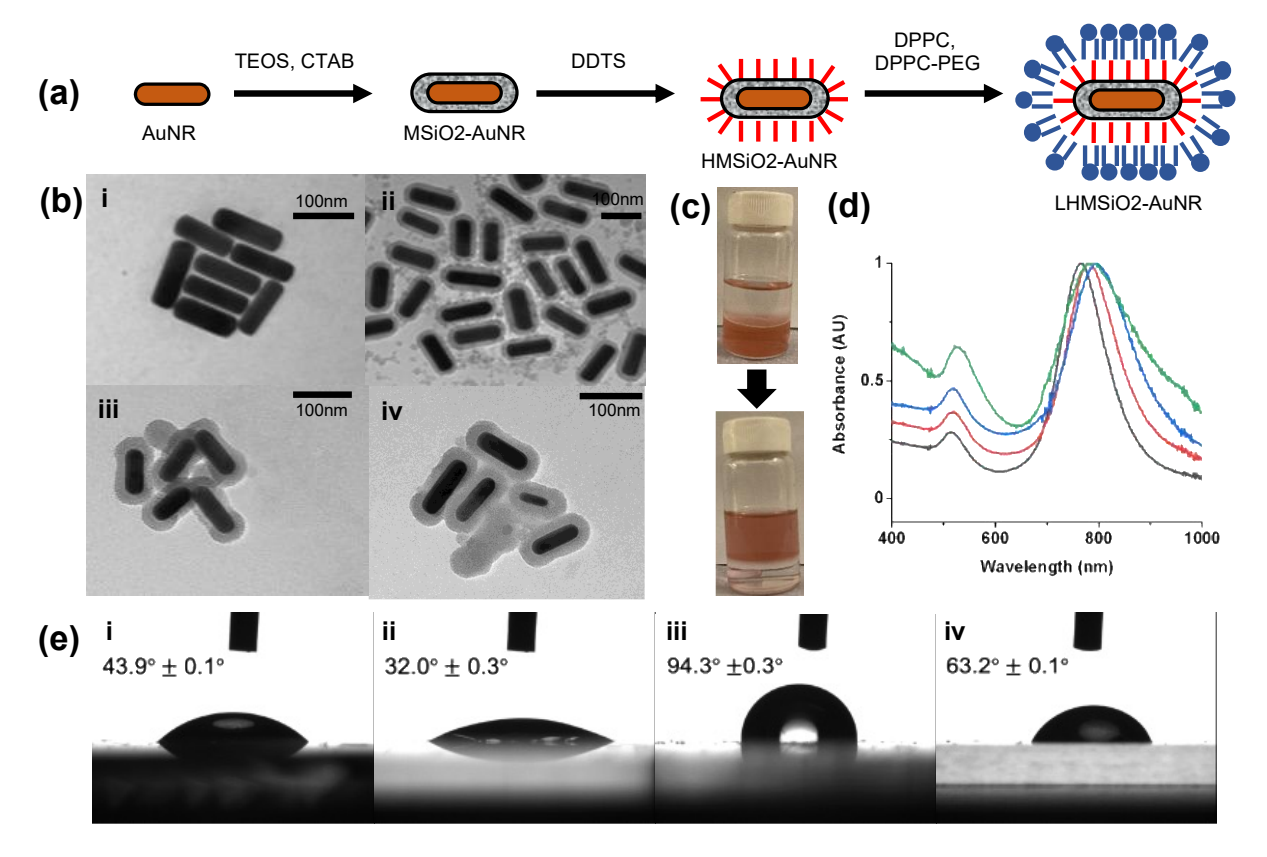


Figure 2. (a) Scheme for synthesis of lipid-coated, hydrophobically-modified mesoporous silica shells on gold nanorods (LHMSiO2-AuNR). (b) TEM images of (i) gold nanorods (AuNR), (ii)

silica coated gold nanorods (MSiO2-AuNR), (iii) hydrophobically modified silica coated gold nanorods (HSiO2-AuNR), and (iv) lipid-coated hydrophobically-modified silica coated gold nanorods (LHMSiO2-AuNR). (c) Photographs of biphasic reaction transfer of MSiO2-AuNR from the acidic methanol layer into the hexane layer through DDTS functionalization to HMSiO2-AuNR. (d) Normalized UV-Vis spectra of AuNR (black curve), MSiO2-AuNR (red curve), HSiO2-AuNR (blue curve), and LHMSiO2-AuNR (green curve). (e) Contact angle measurements of (i) AuNR, (ii) MSiO2-AuNR, (iii) HSiO2-AuNR, and (iv) LHMSiO2-AuNR.

Next, a hydrophobic coating was deposited on the MSiO2-AuNRs to promote bubble stability during the cavitation process.⁴⁵ The remaining bound CTAB was first removed with an acid wash, followed by resuspending the cleaned MSiO2-AuNR across a biphasic mixture of acidified methanol and hexane with dodecyltrichlorosilane (DDTS). Successful hydrophobic modification of the silica coating by DDTS was initially evidenced by a colorimetric phase transfer of the MSiO2-AuNRs from methanol to hexane (Figure 2c). UV-Vis analysis of the hydrophobically modified MSiO2-AuNRs (HMSiO2-AuNRs) showed a shift in the LSPR of about ~15 nm relative to the MSiO2-AuNR before surfactant extraction (Figure 2d), though this spectrum was obtained in chloroform due to insolubility in water. Beyond solubility profile, evidence for successful hydrophobic modification was found by depositing a film of the functionalized AuNRs on a glass surface and measuring the water contact angle (Figure 2e ii and iii). After addition of dodecyl groups to the nanoparticles, the static contact angle of the particles changed from $32.0^{\circ} \pm 0.3^{\circ}$ for the MSiO2-AuNR to $94.3^{\circ} \pm 0.3^{\circ}$ for the HMSiO2-AuNRs (HMSiO2-AuNR) (Figure 2). In addition, FTIR spectroscopy was performed to verify the hydrophobic modification. As shown in Figure S1, peaks were observed for C-H stretching at 2915 cm⁻¹ and 2854 cm⁻¹ and C-H bending at 1376 cm⁻¹. Finally, an increase in average particle size was found by DLS measurements, which showed an increase from 75±30 nm to 137±61 nm, which indicates some possible agglomeration by the particles (Table S1). The zeta potential decreased slightly from -41±1.6 mV to -34±0.8 mV, which is consistent with changing a partially anionic silica layer to the net negatively charged DPPC/DPPC-PEG layer.

Finally, in order to disperse the HMSiO2-AuNR in aqueous media prior to photoacoustic analysis, the hydrophobic particles were coated in a lipid monolayer consisting of 1,2-dipalmitoylphosphatidylcholine (DPPC) and DPPC-polyethylene glycol (DPPC-PEG). Briefly, the HMSiO2-AuNRs were combined with DPPC and DPPC-PEG lipids in chloroform, dried, and rehydrated at 75°C in water. Addition of the lipid monolayer to the surface of the hydrophobically modified mesoporous silica coated gold nanorods (LHMSiO2-AuNR) significantly reduced the static contact angle from $94.3^{\circ} \pm 0.3^{\circ}$ down to $63.2^{\circ} \pm 0.1^{\circ}$ for the LHMSiO2-AuNR, which is consistent with the addition of an amphiphilic lipid to a hydrophobically modified surface. In addition, FTIR spectroscopy showed the presence of a lipid monolayer added to the surface of the HMSiO2-AuNR. As shown in Figure S1, FTIR peaks for DPPC and DPPC-PEG were observed at 1467 cm^{-1} , 1737 cm^{-1} , 2854 cm^{-1} , and 2916 cm^{-1} , corresponding to both C-H and C=O ester peaks.

The photoacoustic signals generated from irradiation of AuNRs, MSiO2-AuNRs, and LHMSiO2-AuNRs were next measured in a standard PA setup (Figure S2). Particles dispersed in water at a concentration of 0.45 nM were flowed at a rate of 80 μL min⁻¹ through a polyethylene tube of 200 μm inner diameter and homogenously irradiated with a nanosecond pulsed laser beam of radius 1.6 mm. Single shots were recorded and averaged 500-1000 times to obtain mean PA signals; examples at 19 mJ cm⁻² are shown in Figure S3. Mean peak-to-peak PA signals (Vpp) as a function of laser fluence were obtained for AuNR (green), MSiO2-AuNR (red), and LHMSiO2-AuNR (black) samples, as well as for the PE tube (magenta) filled with water solvent as a negative

control (Figure 3). As expected, both AuNR and MSiO2-AuNR showed linear trends of PA amplitude vs. fluence up through 21 mJ cm⁻², the largest fluence tested (Figure 3b). In contrast, the trend for LHMSiO2-AuNR particles was distinctly non-linear, fit by 3rd order polynomial (Figure 3b). Without any gold component, no PA response was observed over the tested laser fluence range (Figure S4).

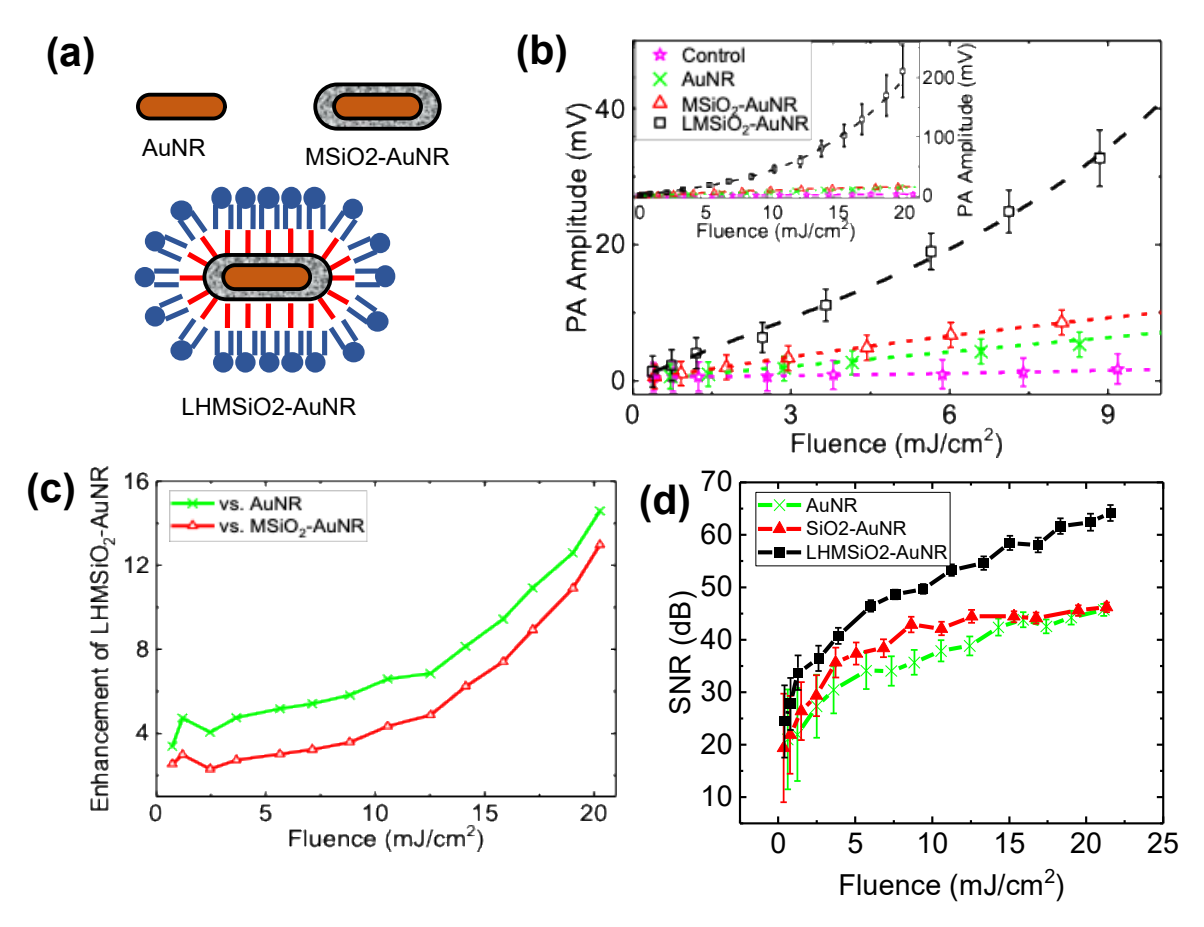


Figure 3. (a) Cartoon schematic of structures tested. (b) PA peak-to-peak amplitude (Vpp) as a function of laser fluence recorded for AuNR (green cross), MSiO2–AuNR (red triangles), and LHMSiO2–AuNR (black squares) particles in water. Signal from the control (PE tube filled with water) is displayed in magenta stars. All particle concentrations were 0.45 nM. Inset shows the results for a wider fluence range. Error bars show one standard deviation in both directions to the mean Vpp; all samples were run in triplicate. The connecting dashed lines show linear fits for

AuNR in green, MSiO2–AuNR in red and for control in magenta. A third order polynomial fit for LHMSiO2–AuNR is displayed in black dashed line. Student's t-test for significance showed p < 0.05 for LHMSiO2-AuNR vs. MSiO2-AuNR at all fluences tested. (c) Enhancement in PA response of LHMSiO2-AuNR vs AuNR (green cross) and MSiO2-AuNR (red triangles) as a function of laser fluence obtained by dividing corresponding amplitudes in Vpp. (d) Signal-to-noise ratios (SNRs) of each sample tested vs. laser fluence. The error bars represent the propagated standard deviations of the signal and noise.

Two trends were immediately apparent: the LHMSiO2-AuNR displayed linear behavior at about 5 mJ cm⁻², and at higher laser fluences the signal increased in a nonlinear manner (Figure 3c). Within the linear portion, the LHMSiO2-AuNR possessed a stronger response to the laser fluence than either MSiO2-AuNR or AuNR, by 2-fold and 3-fold respectively, which was confirmed by comparing the slopes of the PA vs. fluence curve within the linear regime. We hypothesize that the enhancement at lower fluences is caused by the presence of solvent vapor contained within the hydrophobically-modified mesoporous silica pores. At room temperature, air has a thermal expansion coefficient β of \sim 3 x10⁻³ K⁻¹, whereas silica's would be closer to \sim 3 x10⁻⁵ K⁻¹. Thus, increasing the nanorod temperature by laser induced heating may be expected to produce adjacent expansion of encapsulated water vapor that would push against the surrounding medium more strongly, leading to a larger acoustic response. Alternatively, water vapor has a lower thermal conductivity (\sim 0.3 W m⁻¹ K⁻¹) than silica (1.3 W m⁻¹ K⁻¹), which could contribute to the increased PA response.

When fitted to the form of $Ax + Bx^d$, where the Ax comprises the linear component and Bx^d comprises the nonlinear component, the PA signal contained a power term, $d = 3.17 \pm 0.16$, with

an adjusted R² = 0.999 (Figure S5, Table S2). Additionally, a residual sum of the squares (RSS) analysis was performed to compare linear, quadratic, and cubic fits; in doing so, the RSS was reduced from 3571 to 172 to 21, respectively (Table S2). Thus, a cubic fit was most effective at accounting for the relationship between PA response and input laser fluence. The power term is also consistent with that found by Dixon *et al*,³⁹ in which liquid vaporization was facilitated by the presence of microbubbles. The response of LHMSiO2-AuNRs in the nonlinear range resulted in a much stronger photoacoustic response when compared to bare or silica-coated nanorods, which both gave a linear PA response with laser fluence over the whole fluence range (Figure S6). The enhancement increased with laser fluence in the nonlinear regime to a final value of ~13-15 fold at 21 mJ cm⁻². Similarly, the signal-to-noise ratio also increased significantly for LHMSiO2-AuNR, with a value of 64 dB at 21 mJ cm⁻² as compared to 46 dB for both AuNR and MSiO2-AuNR (Figure 3d). In both the linear and nonlinear regimes, the signal enhancement is significant and would translate to improved imaging sensitivity and reduced measurement time.

As observed in the plots in Figure 3, the nonlinear transition in the PA response for the LHMSiO2-AuNR particles was estimated to occur at approximately 5 mJ cm⁻², which is associated with the onset of a liquid-gas phase transformation in the liquid surrounding the nanoparticle. In these studies, AuNR and MSiO₂-AuNR particles did not show evidence of cavitation through a non-linear PA response, indicating that the threshold for cavitation was higher than the fluence range considered in these studies. Both Dixon's and our work observed a transition away from linearity at a similar fluence range, which they attributed to solvent vapor nanobubble formation.³⁹ Here, the presence of rough, hydrophobic surfaces and the corresponding presence of pre-existing gas nuclei reduce the nucleation energy barrier and allow heterogeneous nucleation of solvent vapor. The phase transition of vapor, rather than expansion of air, was shown in a comparison

study between LHMSiO₂-AuNR in air-saturated and degassed water, which showed little difference in terms of PA response (Figure S7). Once phase transformation takes place, a gas bubble can grow rapidly (and potentially collapse) to produce a strong photoacoustic response. The nucleation and growth of a bubble is stochastic and its probability depends on the thermodynamic conditions of a system, such as temperature, gas concentration, and properties of the nucleating surface. S4,55 Murray and others have shown that without an existing gas cavity, laser induced bubble formation begins when the superheated liquid around the nanoparticle approaches the spinodal temperature of water around 550 K. Our results indicate that the local nanoparticle surface conditions can promote heterogeneous nucleation at lower temperatures (decreased laser fluence), which have a dramatic effect on the PA response. When a single volume of LHMSiO₂-AuNRs was irradiated as above and the PA response was monitored at the single shot level, there was an initial decrease in signal followed by a stochastic PA response to the laser (Figure S8). We interpret this result that the pre-existing gas bubbles are initially exhausted, but at later shots, vaporization and then nucleation of new bubbles can take place.

The concentration dependence of the photoacoustic response of the nanoparticles was also explored. Three concentrations of LHMSiO2-AuNRs were prepared: 0.11 nM (1X), 0.21 nM (2X), and 0.32 nM (3X). Not surprisingly, the PA response increased with nanostructure concentration, as more particles were irradiated in a given unit volume (Figure 4). At most laser fluences tested, the enhancement followed the ratio of particle concentrations closely; for example, 3X/2X produced an enhancement of ~1.5. Thus, dependence of PA signal on concentration was found to be roughly linear. This result provides evidence that the observed PA enhancement is likely not due to particle-particle interactions such as overlapping thermal fields or the presence of larger gas pockets stabilized by multiple nanoparticles, as we would expect both effects to be enhanced at

higher concentrations. Because PA response appears linear in concentration but nonlinear in fluence, these nanoparticles may potentially be used to track absolute nanoparticle concentration within the body by, for example, measuring the PA response at two different fluences.^{58,59}

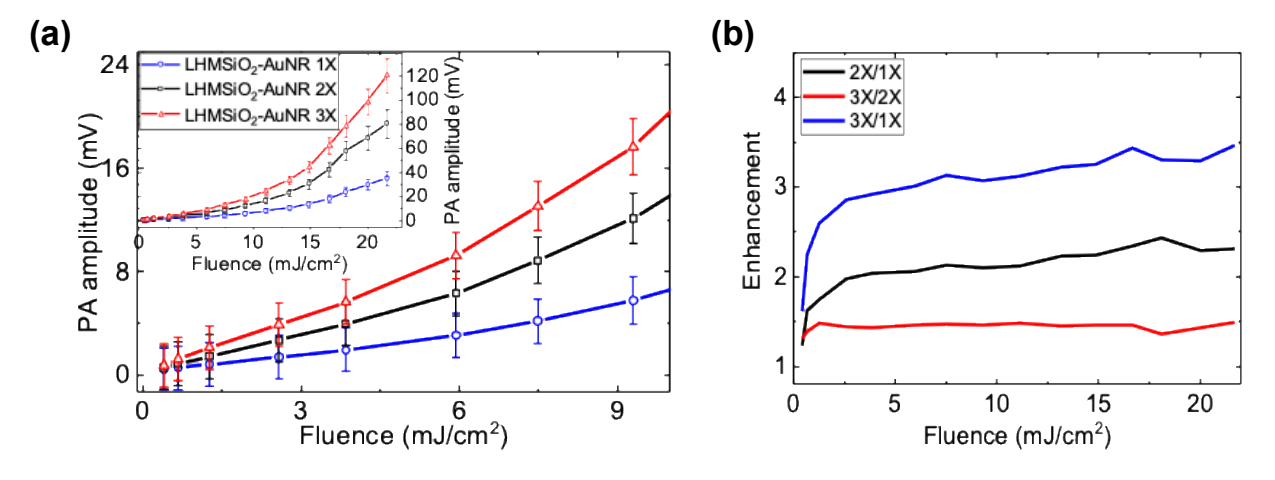


Figure 4. (a) PA response (Vpp) of LHMSiO2-AuNR at varying concentrations: 1 X (0.11nM, blue circles), 2X (0.21nM, black squares) and 3X (0.32nM, red triangles). Inset shows the same results at a broader fluence range. Error bars show 1 standard deviation in both directions to the mean Vpp. **(b)** Enhancement of PA signals for 2X/1X (black), 3X/2X (red) and 3X/1X(blue).

To see how the particles might respond in an environment more akin to the human body, the PA responses of LHMSiO2-AuNR were tested in phosphate buffer saline (PBS), human plasma (HPL), DI water, and bovine serum albumin (BSA) solution. The sample of LHMSiO2-AuNR dispersed in PBS had a PA response that was similar to that obtained in water (Figure 5). However, when LHMSiO2-AuNRs were dispersed in HPL or BSA solution, a PA response was recorded that showed greater nonlinearity, ultimately reaching a two-fold greater PA response than samples in water. This enhancement effect appears to be medium-dependent: AuNRs and MSiO2-AuNRs tested in HPL showed a similar two-fold enhancement in PA (Figure S9), which we hypothesize

occurs because proteins adhering to the nanoparticle surface increase the thermal resistance in the nanorods. Enhancement against AuNR and MSiO2-AuNR was similar, ultimately reaching 17-and 11-fold enhancement respectively at 21 mJ cm⁻². The LHMSiO2-AuNRs also possess low cytotoxicity: after incubation for 48 h and performing an MTT assay, MDA-MB-468 breast cancer cells showed 81±1.2%, 87.3±0.44%, and 94.2±0.5% cell viability at 0.45, 0.045, and 0.0045 nM LHMSiO2-AuNR, respectively (Figure S10).

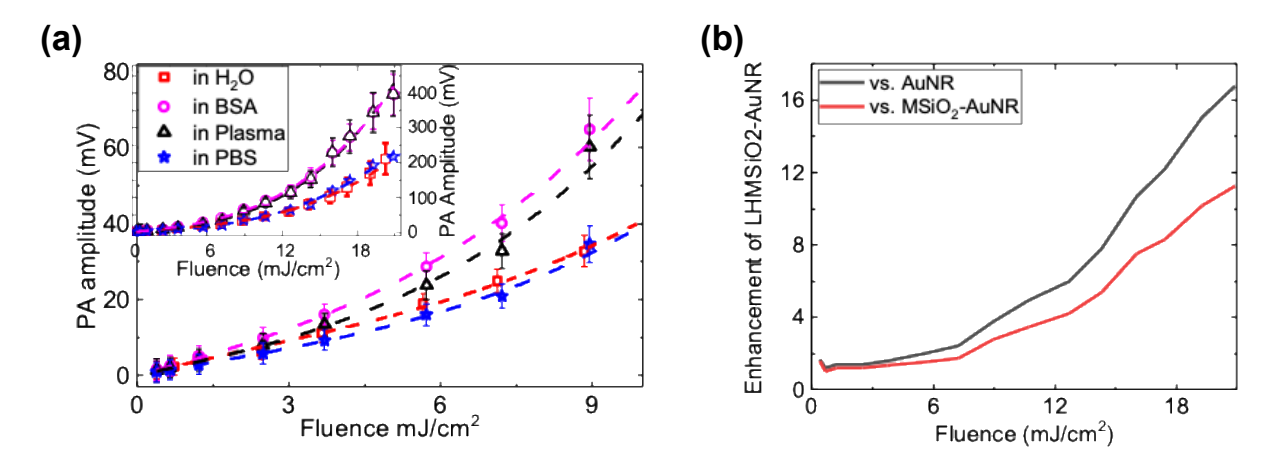


Figure 5. PA response (Vpp) plotted as a function of laser fluence for LHMSiO2-AuNR sample dispersed in water showed in red filled squares; in Bovine Serum Albumin (BSA) displayed in magenta circles; in human plasma (HPL) displayed in black triangle; and in phosphate buffer solution (PBS) displayed in blue star. Dotted lines are from a 3rd order polynomial fit. The inset shows the same results for an extended range of fluences. Error bars show one standard deviation above and below the mean value.

Based on these studies, the likeliest source of heterogeneous nucleation is the entrapment of vapor bubbles inside the hydrophobically-modified pores, which was demonstrated by Goodwin and co-workers for hydrophobically-modified mesoporous silica nanoparticles.²⁶⁻³⁰ If encapsulated vapor were primarily responsible for nonlinear enhancement, rather than the addition

of surfactants capable of stabilizing nascent bubbles, then the addition of lipids without covalent hydrophobic particle modification would not impart significant nonlinearity to the particles. To test this theory, we compared the PA response of LHMSiO2-AuNR with that of MSiO2-AuNR stabilized with a lipid bilayer (LBMSiO2-AuNR), which is known to form around silica nanoparticles to improve their stability and biocompatibility. 60 To determine if hydrophobic modification was necessary for non-linear PA response, a lipid bilayer was added to the MSiO2-AuNR in method similar to that reported in Liu, et al. 60 Briefly, MSiO2-AuNRs were mixed with rehydrated liposomes of DPPC and DPPC-PEG in 0.5X PBS. Static contact angle measurements were performed to characterize the surface of lipid bilayer MSiO2-AuNR, which showed a decrease in contact angle from $23.0^{\circ} \pm 1.0^{\circ}$ to $17.1^{\circ} \pm 0.2^{\circ}$ for the surfactant extracted MSiO2-AuNR and LBMSiO2-AuNR, respectively. The decrease was likely caused by the zwitterionic phosphocholine producing a more hydrophilic surface. Additionally, the negative charge on nanorods became stronger, with zeta potential changing from -26.1 mV to -31.1 mV. Finally, FTIR spectroscopy showed peaks that closely matched with the peaks that were seen in the LHMSiO2-AuNR sample: a C=O stretch at 1738 cm⁻¹, C-H bending at 1467 cm⁻¹, and C-H stretches at 2854 cm⁻¹ and 2915 cm⁻¹ (Figure 6a). These results were distinguished from the LHMSiO2-AuNR by the lower intensity of the C-H stretches.

Once the lipid bilayers were in place, the sample was subjected to the same PA response studies. As seen in Figure 6b, while LHMSiO2-AuNR achieves a nonlinear value, the LBMSiO2-AuNR sample is still linear. Thus, the hydrophobic modification plays a dominant role in the nonlinear relationship between PA response and laser fluence. The hydrophobic modification also improved the stability of the irradiated rods. As shown in Figure S11, TEM images of LHMSiO2-AuNRs recovered from water one month after irradiation showed little degradation of either the gold (from

melting) or silica (from hydrolysis). In contrast, AuNRs showed significant deformation, as expected from melting by laser heating. Similarly, while silica coatings on MSiO₂-AuNR were completely dissolved within 5 days, the LHMSiO₂-AuNR showed no degradation within one week (Figure S12).

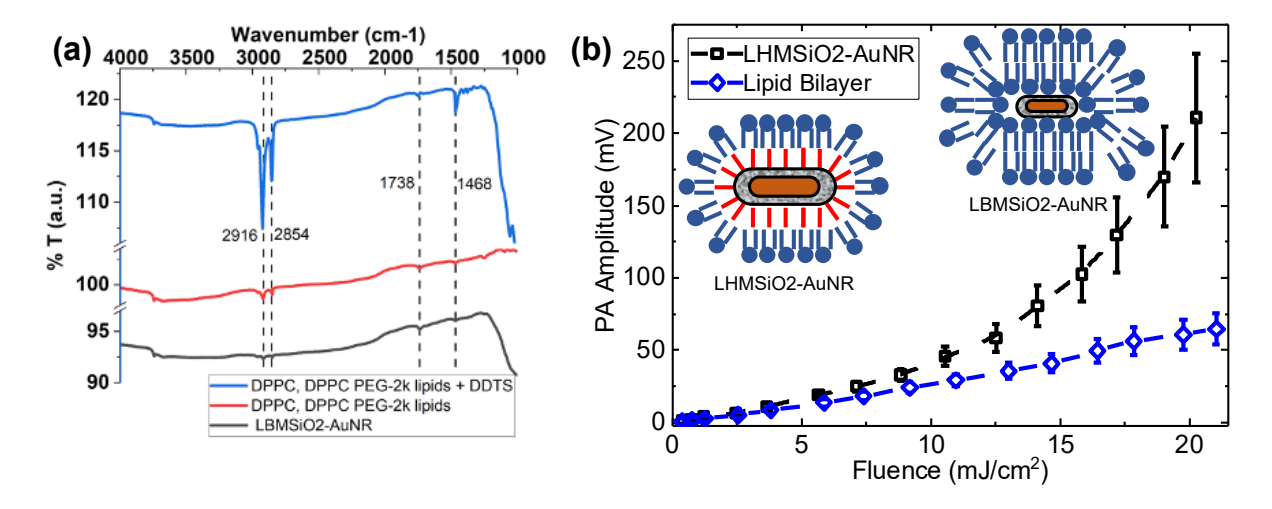


Figure 6. (a) FTIR spectra showing the presence of lipid bilayers on LBMSiO2-AuNR. (b) PA response as a function of fluence observed for LHMSiO2-AuNR particles coated with lipid bilayer (blue circles). PA response of LHMSiO2-AuNR (lipid monolayer) is also displayed for comparison. Water was used as the solvent in both cases. Error bars show one standard deviation above and below the mean value. Student's t-test for significance showed p < 0.05 for LHMSiO2-AuNR vs. LBMSiO2-AuNR at all fluences tested.

In conclusion, the lipid-coated, hydrophobically-modified gold nanorods (LHMSiO2₂-AuNR) presented here exhibit a nonlinear PA response with laser fluence at relatively low laser fluences. In functionalizing nanorods with hydrophobic, porous silica, vapor channels could be maintained in the pores that could facilitate the liquid-vapor transition of surrounding solvent and promote nonlinear enhancement. At low fluences, enhancement was observed due to either the increased thermal expansion coefficient or increased thermal resistance of the rods.^{29,61} At higher fluences,

the data fit exponential curves that were consistent with data reported for microbubbles. The reported nanoparticles showed an approximately linear relationship between PA response and concentration, which allows the response to be distinguished in terms of either laser fluence or concentration. Finally, the LHMSiO2-AuNRs exhibited strong enhancement in human plasma, which shows promise for future *in vivo* imaging studies. Overall, this approach of hydrophobic functionalization of a mesoporous silica shell can be applied to many different types of nanostructures and represents a potential platform technology for imparting nonlinearity to other photoacoustic contrast agents at laser fluences compatible with *in vivo* imaging.

Methods

Synthesis of gold nanorods (AuNRs). Gold nanorods were produced with a method that required the production of separate growth and seed solutions.¹⁷ The growth solution was was started by combining 0.7 g of cetrimmonium bromide (CTAB) and 25 mL of ultrapure water and dissolved by heating. Next, 0.1234 g of sodium oleate (NaOL) was added and dissolved by heating the solution. The solution was then cooled to 30°C for 15 min. 2.4 mL of 4 mM silver nitrate was added and left undisturbed for 15 min. Finally, 25 mL of 1 mM gold (III) trihydride HAuCl4 was added to the solution, which was mixed at 200 rpm for 90 min at 30°C.

While the growth solution was mixing, the seed solution was made by adding 1 mL of 0.5 mM HAuCl₄ and 1 mL of 0.2 M CTAB to a 4 mL borosilicate vial. 200 μl of 0.0006 M NaBH₄ in ice cold water is then added to the seed solution and stirred vigorously for 2 min. The seed solution was then aged for 30 min at RT. When the seed solution became clear, 175 μL of 37% hydrochloric acid (HCl) was added and the solution was mixed for 15 min. 125 μL of a 0.064 M ascorbic acid was added to the growth solution and the growth solution was stirred vigorously at room

temperature for 30 s. Finally, 40 µL of the seed solution was added to the growth solution and left at 30°C for 12 h. After the reaction, the gold nanorods were centrifuge washed twice at 7500g for 20 min to remove excess CTAB.

Synthesis of mesoporous silica coated gold nanorods (MSiO₂-AuNRs). The AuNRs were diluted to 1 nM with water and 90 μ l of 20 mM CTAB to create a 1 mL aqueous suspension of 1 nM AuNRs. The colloidal suspension was mixed for 12 h in a 4 mL borosilicate vial. 10 μ l of 0.1 M sodium hydroxide (NaOH) was added, and the suspension was stirred vigorously for 30 min. 36 μ l of a 5% volume solution of tetraethylorthosilicate (TEOS) dispersed in isopropoyl alocohol (IPA) was added to the suspension in four 9 μ L doses over a 90 min period. The solution was then mixed overnight and centrifuged at 6708g for 15 min. To redisperse the nanoparticles, methanol was added, and the mixture was bath sonicated.

Extraction of CTAB from MSiO2-AuNRs. 80 μL of 37% HCl was added to 10 mL of MSiO2-AuNRs dispersed in methanol in a 20 mL borosilicate vial. The suspension was heated to and mixed at 65°C for 1 h. The sample was then centrifuged at 6708g for 15 min. The pellet was redispersed in methanol and the centrifuge washing was repeated twice to neutralize the sample for later storage.

Synthesis of hydrophobically modified mesoporous silica coated gold nanorods (HMSiO₂-AuNRs). 80 μL of 37% HCl was added to a suspension of MSiO₂-AuNRs dispersed in methanol. 8 mL of hexane was added to the solution. 500 μL dodecyltrichlorosilane was then added in five 100 μL portions to the mixture, which was capped and sealed with Parafilm and mixed vigorously for 5 h. The sample was then centrifuge washed twice with hexane and twice with chloroform. The sample was re-dispersed in 8 mL of chloroform and stored as a suspension.

Preparation of lipid-coated hydrophobically modified mesoporous silica coated gold nanorods (LHMSiO₂-AuNRs). 300μL DPPC (4 mg mL⁻¹) and 200 μL DPPC-PEG2000 (2 mg mL⁻¹), each of which was dispersed in chloroform, then added to a suspension of HMSiO₂-AuNRs in chloroform. The sample was evaporated at 65°C, re-dispersed in 8 mL of water, then mixed for 45 min at 65°C. The sample was collected as a pellet by centrifugation at 6700g and redispersed in water for PA measurement.

Preparation of lipid-bilayer mesoporous silica coated gold nanorods (LBMSiO₂-AuNRs). 500 μL of 4 mg mL⁻¹ DPPC in chloroform was added to 300 μL of 2 mg mL⁻¹ DPPC and DPPC-PEG dispersed in chloroform. These samples were then dried under a stream of inert argon until the chloroform was evaporated. The liposomes were rehydrated in 1 mL 0.5X PBS at ~60°C for 1 h. The liposomes were sonicated with a probe sonicator for 1 min in a 10 second on and 10 second off cycle. 2 mL of CTAB-extracted MSiO₂-AuNR suspension (see above) was centrifuged at 6708g for 15 min and redispersed in 0.5X PBS. The liposomes were then added to the CTAB-extracted MSiO₂-AuNR and left at room temperature for 1 h. The lipid bilayer MSiO₂-AuNR was then centrifuged at 6700g for 15 min and centrifuge washed an additional two times with water.

Characterization of nanorods by UV-Vis spectroscopy. The AuNR concentration was first determined utilizing the maximum absorbance peak to determine the extinction coefficient from Orendorff et. al.⁴⁹ The concentrations of other AuNR derivatives were then determined assuming AuNR as the only absorber and scatterer in the NIR.

FTIR measurements. The FTIR measurements were performed using a Nicolet 6700 ATR. The colloidal solution was deposited onto a clean microscope glass slide, and then dried in an oven at 85 °C overnight. The sample was then placed on an ATR crystal and analyzed.

Contact angle measurements. The contact angle measurements were performed utilizing a Rame-Hart 210-U1 Goniometer. To form the surfaces for measurement, the colloidal solutions were deposited onto a clean glass microscope slide, and then dried at 85 °C overnight to remove excess solvent.

Transmission electron microscopy (TEM) images. TEM images were taken with a Technai T12 Spirit.

Measurements of dynamic light scattering (DLS) and zeta potential. For DLS, 1 mL of AuNR, MSiO2-AuNR, or LHMSiO2-AuNR in ultrapure water was added to a disposable semi micro UV-cuvette. Using a Litesizer 500 with the particle size software, measurements were performed at 25°C. For zeta potential measurements, 300 μL suspension was added to an Omega cuvette Using a Litesizer 500 with the zeta potential analysis software, the zeta potential was measured at 25°C utilizing the Smoluchowski approximation..

Measurements of photoacoustic response. Photoacoustic response of the synthesized particles was analyzed in a standard setup (Figure S2). An Optical Parametric Oscillator pumped by a Q-switched laser (model: SLI-20, Continuum Electro-Optics, Inc. 3150 Central Expressways, Santa Clara CA95051) with pulse repetition rate 20 Hz, tuned to operate at a chosen wavelength corresponding to the peak absorption of the sample (S) flowing through a transparent polyethylene tube (SCI Cat. # BB31695-PE/C 0.20mm x 0.36mm - inner x outer diameter) lie at the center of laser beam waist of radius 1.4 – 1.6 mm (at 1/e), at the focus of a lens (L3, focus = 25 cm). A mirror (M) was used to direct beam towards the sample and an engineered diffuser (D) was used to homogenize laser beam profile in order to avoid hotspots. Filter (F) blocks the fundamental (532 nm) wavelength from laser and allows to pass near infrared laser wavelengths. L1 and L2 (5 cm and 15 cm focal lengths, respectively) was used to expand the incoming beam to obtain a desired

beam waist at the sample location. Wave plate (WP) along with the polarizing beam splitter cube (PBS) were used to control the laser energy hits in the sample. N is a neutral density filter for reducing laser power to an energy meter (EM, Thorlabs PM100D console and ES111C energy sensor).

A syringe pump (Harvard Apparatus, PhD Ultra) was in place to infuse particles in solution through the 200 μm inner diameter polyethylene tube (Cat.# BB31695-PE/C; Dimensions: I.D. x O.D.: 0.20 mm x 0.36 mm; Scientific Commodities, 2800 Sweetwater Ave., A105, Lake Havasu City, AZ 86406) in a controlled flow rate of 80 μL min⁻¹, which was calculated to avoid repeated exposure of a flowing particles to subsequent laser pulses. For the single-shot fatigue experiments, no flow was applied in the tubing (see Figure S8). For long-term stability studies, S was collected post-irradiation for later analysis.

An ultrasound transducer (T), with focal length 19 mm and 10 MHz central frequency (Panametrics, V327) was used to capture the PA signal emitted by S. A water bath was used to facilitate acoustic coupling between S and T. Acoustic signals corresponding to each laser shots converted into electric pulses by T was pre-amplified (FEMTO, high speed GHz amplifier HSA-Y), and finally detected and digitized using an oscilloscope (Telydyne Lecroy, Model HDO4032) and stored into a computer. The EM was used to monitor pulse to pulse laser energy and a photodetector (PD) exposed to the beam reflected through a 2 mm thick microscope slide glass plate (G) was used to trigger the oscilloscope. A home-made data acquisition software using LabVIEW (NI, 11500 N Mopac Expwy, Austin, TX 78759-3504) was used to automize the experiments.

In order to ensure that the sample would behave as homogenous and randomly packed point absorbers, the particles were flowed through a transparent tube of inner diameter $200 \mu m$ and

quasi-homogeneously irradiated by Gaussian profile laser pulses of 3 mm in diameter.⁶² In order to obtain PA signals as a function of fluence, laser pulse energy was adjusted using a waveplate combined with a polarizing beam splitter. For each sample, irradiation fluence was varied from 1 to 25 mJ cm⁻² to match clinically relevant fluence levels. PA response for up to 1000 single shots of laser irradiation was captured at the lowest fluences to enhance the signal to noise ratio (SNR). The number of averages were decreased as the fluence level increased so that for the highest fluence only 300 single shot responses were captured. The tube wall absorption was negligible as evidenced by signals measured in water alone (Figure S3).

Degassed water experiments. Water was degassed by heating water until it boiled and then letting it cool back to RT. The water was then sealed with Parafilm with minimal headspace. A suspension LHMSiO2-AuNR was then created as reported above, except the particles were washed 3x with degassed with water. The degassed water experiments were performed the same way as the main photoacoustic experiments.

Statistical analysis. Utilizing Origin 2020b (OriginLab), a best fit was performed utilizing a nonlinear curve fit of Ax+Bx^d. In this statistical analysis, the goodness of fit was determined (R^2), as well as the residual sum of squares (RSS) for the nonlinear curve as well as to a linear, quadratic, and a cubic fit.

MDA-MB-468 Cell Viability Assay for LHMSiO2-AuNR Nanoparticles. MDA-MB-468 breast carcinoma cells were procured from the American Type Culture Collection (ATCC) and grown to confluence in 75 cm² culture flasks at 37°C under 5% CO₂ in the presence of Dulbecco's Modified Eagle Media (DMEM, with glucose and glutamine, phenol red but no sodium pyruvate, Gibco) supplemented with 10% fetal bovine serum (FBS, Gibco) and 1% penicillin-streptomycin (Thermo Fisher). The cells were then trypsinized with 0.025% Trypsin-EDTA (Gibco), seeded in 12 wells

cells were washed with 100 μ L PBS twice, and then 100 μ L of 0.45, 0.045, or 0.0045 nM of LHMSiO2-AuNR nanoparticle solution in DMEM media was added to the wells. Each nanoparticle concentration variant was studied in triplicate. As a control, fresh media was added instead of the nanorod suspension. After 48 h of incubation, cells were washed with 100 μ L PBS thrice. 100 μ L of 0.5 mg/ml MTT (3-(4,5-dimethylthiazol-2-yl)-2,5-diphenyltetrazolium bromide)

of a 96 well cell culture plate with 10000 cells/well seeding density, and grown for 48 h. Next,

was adding to the media in each of the wells. After incubating MTT solution to the cells for 4h,

the formazan crystals were dissolved by adding isopropanol. Then UV absorbance of the wells

was measured in a SynergyH1 microplate reader (BioTek, USA). Each of the absorbance values

at 560 nm were background corrected by subtracting the reading at 650 nm from that of the 560

nm reading. Then, considering the UV absorbance of the control cells as 100% viable, the viability

fraction of other variants was calculated.

ASSOCIATED CONTENT

Supporting Information. Additional FTIR spectra of nanorods, schematic of photoacoustic

setup, typical pulse shapes, fits of PA vs. laser fluence data to models, PA response for control

samples, PA response of sample without flow, TEM images of irradiated rods.

AUTHOR INFORMATION

Corresponding Author

*Email: andrew.goodwin@colorado.edu, Jennifer.cha@colorado.edu, todd.murray@colorado.edu

23

Author Contributions

The manuscript was written through contributions of all authors. All authors have given approval to the final version of the manuscript. ‡These authors contributed equally.

Funding Sources

NIH R21EB027319, NSF CBET 2025547.

ACKNOWLEDGMENT

The authors acknowledge NIH R21EB027319 and NSF CBET 2025547 for support of this research. The authors thank Prof. Will Medlin for use of his FTIR spectrometer. Finally, the authors thank Fan Yang and Dr. Nicholas Blum for helpful discussions regarding silica-coated nanorod synthesis.

ABBREVIATIONS

AuNR, gold nanorod; BSA, bovine serum albumin; CTAB, cetrimonium bromide; DDTS, dodecyltrichlorosilane; DI, deionized; DPPC, 1,2-dipalmitoylphosphatidylcholine; FTIR, Fourier Transform Infrared; HCl, hydrochloric acid; HPL, human plasma; HSiO2-AuNR, hydrophobically modified silica coated gold nanorods; LBMSiO2-AuNR, lipid bilayer stabilized mesoporous silica coated gold nanorod; LHMSiO2, lipid-coated, hydrophobically-modified mesoporous silica; LSPR, localized surface plasmonic resonance; MSiO2, mesoporous silica; MSiO2-AuNR, mesoporous silica coated gold nanorods; NaOL, sodium oleate; PA, photoacoustic; PBS, phosphate buffered saline; PEG, polyethylene glycol; TEM, transmission

electron microscopy; TEOS, tetraethylorthosilicate; UV-Vis, UV and visible; Vpp, peak-to-peak voltage; WP, waveplate.

REFERENCES

- (1) Beard, P. Biomedical Photoacoustic Imaging. *Interface Focus* **2011**, *1* (4), 602–631. https://doi.org/10.1098/rsfs.2011.0028.
- (2) Manohar, S.; Dantuma, M. Current and Future Trends in Photoacoustic Breast Imaging. *Photoacoustics* **2019**, *16*, 100134. https://doi.org/10.1016/j.pacs.2019.04.004.
- (3) Emelianov, S. Y.; Li, P.-C.; O'Donnell, M. Photoacoustics for Molecular Imaging and Therapy. *Phys. Today* **2009**, *62* (8), 34–39.
- (4) Laufer, J. G.; Zhang, E. Z.; Treeby, B. E.; Cox, B. T.; Beard, P. C.; Johnson, P.; Pedley, B. In Vivo Preclinical Photoacoustic Imaging of Tumor Vasculature Development and Therapy. *J. Biomed. Opt.* **2012**, *17* (5), 1. https://doi.org/10.1117/1.JBO.17.5.056016.
- (5) Wang, L. V.; Hu, S. Photoacoustic Tomography: In Vivo Imaging from Organelles to Organs. *Science* **2012**, *335* (6075), 1458–1462. https://doi.org/10.1126/science.1216210.
- (6) Zhang, H. F.; Maslov, K.; Stoica, G.; Wang, L. V. Functional Photoacoustic Microscopy for High-Resolution and Noninvasive in Vivo Imaging. *Nat. Biotechnol.* **2006**, *24* (7), 848–851. https://doi.org/10.1038/nbt1220.
- (7) Conkey, D. B.; Caravaca-Aguirre, A. M.; Dove, J. D.; Ju, H.; Murray, T. W.; Piestun, R. Super-Resolution Photoacoustic Imaging through a Scattering Wall. *Nat. Commun.* **2015**, *6* (1), 7902. https://doi.org/10.1038/ncomms8902.
- (8) Xu, M.; Wang, L. V. Photoacoustic Imaging in Biomedicine. *Rev. Sci. Instrum.* **2006**, 77 (4), 041101. https://doi.org/10.1063/1.2195024.
- (9) Xia, J.; Yao, J.; Wang, L. V. Photoacoustic Tomography: Principles and Advances. *Electromagn. Waves Camb. Mass* **2014**, *147*, 1–22. https://doi.org/10.2528/pier14032303.
- (10) Weber, J.; Beard, P. C.; Bohndiek, S. E. Contrast Agents for Molecular Photoacoustic Imaging. *Nat. Methods* **2016**, *13* (8), 639–650. https://doi.org/10.1038/nmeth.3929.
- (11) Upputuri, P. K.; Pramanik, M. Recent Advances in Photoacoustic Contrast Agents for in Vivo Imaging. *WIREs Nanomedicine Nanobiotechnology* **2020**, *12* (4). https://doi.org/10.1002/wnan.1618.
- (12) Kang, J.; Kim, D.; Wang, J.; Han, Y.; Zuidema, J. M.; Hariri, A.; Park, J.-H.; Jokerst, J. V.; Sailor, M. J. Enhanced Performance of a Molecular Photoacoustic Imaging Agent by Encapsulation in Mesoporous Silicon Nanoparticles. *Adv. Mater.* **2018**, *30* (27), 1800512. https://doi.org/10.1002/adma.201800512.
- (13) Luke, G. P.; Yeager, D.; Emelianov, S. Y. Biomedical Applications of Photoacoustic Imaging with Exogenous Contrast Agents. *Ann. Biomed. Eng.* **2012**, *40* (2), 422–437. https://doi.org/10.1007/s10439-011-0449-4.
- (14) Li, W.; Chen, X. Gold Nanoparticles for Photoacoustic Imaging. *Nanomed.* **2015**, *10* (2), 299–320. https://doi.org/10.2217/nnm.14.169.
- (15) Manohar, S.; Ungureanu, C.; Van Leeuwen, T. G. Gold Nanorods as Molecular Contrast Agents in Photoacoustic Imaging: The Promises and the Caveats: GOLD NANORODS IN

- PHOTOACOUSTIC MOLECULAR IMAGING. *Contrast Media Mol. Imaging* **2011**, *6* (5), 389–400. https://doi.org/10.1002/cmmi.454.
- (16) Wu, D.; Huang, L.; Jiang, M.; Jiang, H. Contrast Agents for Photoacoustic and Thermoacoustic Imaging: A Review. *Int. J. Mol. Sci.* **2014**, *15* (12), 23616–23639. https://doi.org/10.3390/ijms151223616.
- (17) Lyu, Y.; Fang, Y.; Miao, Q.; Zhen, X.; Ding, D.; Pu, K. Intraparticle Molecular Orbital Engineering of Semiconducting Polymer Nanoparticles as Amplified Theranostics for *in Vivo* Photoacoustic Imaging and Photothermal Therapy. *ACS Nano* **2016**, *10* (4), 4472–4481. https://doi.org/10.1021/acsnano.6b00168.
- (18) Zhen, X.; Feng, X.; Xie, C.; Zheng, Y.; Pu, K. Surface Engineering of Semiconducting Polymer Nanoparticles for Amplified Photoacoustic Imaging. *Biomaterials* **2017**, *127*, 97–106. https://doi.org/10.1016/j.biomaterials.2017.03.003.
- (19) Huang, J.; Pu, K. Activatable Molecular Probes for Second Near-Infrared Fluorescence, Chemiluminescence, and Photoacoustic Imaging. *Angew. Chem. Int. Ed.* **2020**, *59* (29), 11717–11731. https://doi.org/10.1002/anie.202001783.
- (20) Amendola, V.; Pilot, R.; Frasconi, M.; Maragò, O. M.; Iatì, M. A. Surface Plasmon Resonance in Gold Nanoparticles: A Review. *J. Phys. Condens. Matter* **2017**, *29* (20), 203002. https://doi.org/10.1088/1361-648X/aa60f3.
- (21) Ye, X.; Zheng, C.; Chen, J.; Gao, Y.; Murray, C. B. Using Binary Surfactant Mixtures To Simultaneously Improve the Dimensional Tunability and Monodispersity in the Seeded Growth of Gold Nanorods. *Nano Lett.* **2013**, *13* (2), 765–771. https://doi.org/10.1021/nl304478h.
- (22) Chen, Y.-S.; Frey, W.; Kim, S.; Homan, K.; Kruizinga, P.; Sokolov, K.; Emelianov, S. Enhanced Thermal Stability of Silica-Coated Gold Nanorods for Photoacoustic Imaging and Image-Guided Therapy. *Opt. Express* **2010**, *18* (9), 8867. https://doi.org/10.1364/OE.18.008867.
- (23) Kong, F.; Silverman, R. H.; Liu, L.; Chitnis, P. V.; Lee, K. K.; Chen, Y. C. Photoacoustic-Guided Convergence of Light through Optically Diffusive Media. *Opt. Lett.* **2011**, *36* (11), 2053. https://doi.org/10.1364/OL.36.002053.
- (24) Lai, P.; Wang, L.; Tay, J. W.; Wang, L. V. Photoacoustically Guided Wavefront Shaping for Enhanced Optical Focusing in Scattering Media. *Nat. Photonics* **2015**, *9* (2), 126–132. https://doi.org/10.1038/nphoton.2014.322.
- (25) Chaigne, T.; Katz, O.; Boccara, A. C.; Fink, M.; Bossy, E.; Gigan, S. Controlling Light in Scattering Media Non-Invasively Using the Photoacoustic Transmission Matrix. *Nat. Photonics* **2014**, *8* (1), 58–64. https://doi.org/10.1038/nphoton.2013.307.
- (26) Tzang, O.; Caravaca-Aguirre, A. M.; Wagner, K.; Piestun, R. Adaptive Wavefront Shaping for Controlling Nonlinear Multimode Interactions in Optical Fibres. *Nat. Photonics* **2018**, *12* (6), 368–374. https://doi.org/10.1038/s41566-018-0167-7.
- (27) Mantri, Y.; Jokerst, J. V. Engineering Plasmonic Nanoparticles for Enhanced Photoacoustic Imaging. *ACS Nano* **2020**, *14* (8), 9408–9422. https://doi.org/10.1021/acsnano.0c05215.
- (28) Gao, F.; Bai, L.; Liu, S.; Zhang, R.; Zhang, J.; Feng, X.; Zheng, Y.; Zhao, Y. Rationally Encapsulated Gold Nanorods Improving Both Linear and Nonlinear Photoacoustic Imaging Contrast in Vivo. *Nanoscale* **2017**, *9* (1), 79–86. https://doi.org/10.1039/C6NR07528B.
- (29) Chen, Y.-S.; Frey, W.; Kim, S.; Kruizinga, P.; Homan, K.; Emelianov, S. Silica-Coated Gold Nanorods as Photoacoustic Signal Nanoamplifiers. *Nano Lett.* **2011**, *11* (2), 348–354. https://doi.org/10.1021/nl1042006.

- (30) Inose, T.; Oikawa, T.; Shibuya, K.; Tokunaga, M.; Hatoyama, K.; Nakashima, K.; Kamei, T.; Gonda, K.; Kobayashi, Y. Fabrication of Silica-Coated Gold Nanorods and Investigation of Their Property of Photothermal Conversion. *Biochem. Biophys. Res. Commun.* **2017**, *484* (2), 318–322. https://doi.org/10.1016/j.bbrc.2017.01.112.
- (31) Jokerst, J. V.; Thangaraj, M.; Kempen, P. J.; Sinclair, R.; Gambhir, S. S. Photoacoustic Imaging of Mesenchymal Stem Cells in Living Mice via Silica-Coated Gold Nanorods. *ACS Nano* **2012**, *6* (7), 5920–5930. https://doi.org/10.1021/nn302042y.
- (32) Farny, C. H.; Wu, T.; Holt, R. G.; Murray, T. W.; Roy, R. A. Nucleating Cavitation from Laser-Illuminated Nano-Particles. *Acoust. Res. Lett. Online* **2005**, *6* (3), 138–143. https://doi.org/10.1121/1.1897823.
- (33) Kotaidis, V.; Dahmen, C.; von Plessen, G.; Springer, F.; Plech, A. Excitation of Nanoscale Vapor Bubbles at the Surface of Gold Nanoparticles in Water. *J. Chem. Phys.* **2006**, *124* (18), 184702. https://doi.org/10.1063/1.2187476.
- (34) Lukianova-Hleb, E. Y.; Santiago, C.; Wagner, D. S.; Hafner, J. H.; Lapotko, D. O. Generation and Detection of Plasmonic Nanobubbles in Zebrafish. *Nanotechnology* **2010**, 21 (22), 225102. https://doi.org/10.1088/0957-4484/21/22/225102.
- (35) Lukianova-Hleb, E. Y.; Koneva, I. I.; Oginsky, A. O.; La Francesca, S.; Lapotko, D. O. Selective and Self-Guided Micro-Ablation of Tissue with Plasmonic Nanobubbles. *J. Surg. Res.* **2011**, *166* (1), e3–e13. https://doi.org/10.1016/j.jss.2010.10.039.
- (36) Peeters, S.; Kitz, M.; Preisser, S.; Wetterwald, A.; Rothen-Rutishauser, B.; Thalmann, G. N.; Brandenberger, C.; Bailey, A.; Frenz, M. Mechanisms of Nanoparticle-Mediated Photomechanical Cell Damage. *Biomed. Opt. Express* **2012**, *3* (3), 435. https://doi.org/10.1364/BOE.3.000435.
- (37) Wei, C.; Xia, J.; Lombardo, M.; Perez, C.; Arnal, B.; Larson-Smith, K.; Pelivanov, I.; Matula, T.; Pozzo, L.; O'Donnell, M. Laser-Induced Cavitation in Nanoemulsion with Gold Nanospheres for Blood Clot Disruption: In Vitro Results. *Opt. Lett.* **2014**, *39* (9), 2599. https://doi.org/10.1364/OL.39.002599.
- (38) Wilson, K.; Homan, K.; Emelianov, S. Biomedical Photoacoustics beyond Thermal Expansion Using Triggered Nanodroplet Vaporization for Contrast-Enhanced Imaging. *Nat. Commun.* **2012**, *3* (1), 618. https://doi.org/10.1038/ncomms1627.
- (39) Dixon, A. J.; Hu, S.; Klibanov, A. L.; Hossack, J. A. Oscillatory Dynamics and In Vivo Photoacoustic Imaging Performance of Plasmonic Nanoparticle-Coated Microbubbles. *Small* **2015**, *11* (25), 3066–3077. https://doi.org/10.1002/smll.201403398.
- (40) Wei, C.; Lombardo, M.; Larson-Smith, K.; Pelivanov, I.; Perez, C.; Xia, J.; Matula, T.; Pozzo, D.; O'Donnell, M. Nonlinear Contrast Enhancement in Photoacoustic Molecular Imaging with Gold Nanosphere Encapsulated Nanoemulsions. *Appl. Phys. Lett.* **2014**, *104* (3), 033701. https://doi.org/10.1063/1.4862461.
- (41) Blum, N. T.; Yildirim, A.; Gyorkos, C.; Shi, D.; Cai, A.; Chattaraj, R.; Goodwin, A. P. Temperature-Responsive Hydrophobic Silica Nanoparticle Ultrasound Contrast Agents Directed by Phospholipid Phase Behavior. *ACS Appl. Mater. Interfaces* **2019**, *11* (17), 15233–15240. https://doi.org/10.1021/acsami.8b22659.
- (42) Yildirim, A.; Shi, D.; Roy, S.; Blum, N. T.; Chattaraj, R.; Cha, J. N.; Goodwin, A. P. Nanoparticle-Mediated Acoustic Cavitation Enables High Intensity Focused Ultrasound Ablation Without Tissue Heating. *ACS Appl. Mater. Interfaces* **2018**, *10* (43), 36786–36795. https://doi.org/10.1021/acsami.8b15368.

- (43) Yildirim, A.; Chattaraj, R.; Blum, N. T.; Shi, D.; Kumar, K.; Goodwin, A. P. Phospholipid Capped Mesoporous Nanoparticles for Targeted High Intensity Focused Ultrasound Ablation. *Adv. Healthc. Mater.* **2017**, *6* (18). https://doi.org/10.1002/adhm.201700514.
- (44) Bull, D. S.; Nelson, N.; Konetski, D.; Bowman, C. N.; Schwartz, D. K.; Goodwin, A. P. Contact Line Pinning Is Not Required for Nanobubble Stability on Copolymer Brushes. *J. Phys. Chem. Lett.* **2018**, *9* (15), 4239–4244. https://doi.org/10.1021/acs.jpclett.8b01723.
- (45) Yildirim, A.; Chattaraj, R.; Blum, N. T.; Goodwin, A. P. Understanding Acoustic Cavitation Initiation by Porous Nanoparticles: Toward Nanoscale Agents for Ultrasound Imaging and Therapy. *Chem. Mater.* **2016**, *28* (16), 5962–5972. https://doi.org/10.1021/acs.chemmater.6b02634.
- (46) Kuriakose, M.; Borden, M. A. Microbubbles and Nanodrops for Photoacoustic Tomography. *Curr. Opin. Colloid Interface Sci.* **2021**, *55*, 101464. https://doi.org/10.1016/j.cocis.2021.101464.
- (47) Gao, R.; Xu, Z.; Ren, Y.; Song, L.; Liu, C. Nonlinear Mechanisms in Photoacoustics—Powerful Tools in Photoacoustic Imaging. *Photoacoustics* **2021**, *22*, 100243. https://doi.org/10.1016/j.pacs.2021.100243.
- (48) Zhang, Z.; Wang, L.; Wang, J.; Jiang, X.; Li, X.; Hu, Z.; Ji, Y.; Wu, X.; Chen, C. Mesoporous Silica-Coated Gold Nanorods as a Light-Mediated Multifunctional Theranostic Platform for Cancer Treatment. *Adv. Mater.* **2012**, *24* (11), 1418–1423. https://doi.org/10.1002/adma.201104714.
- (49) Orendorff, C. J.; Murphy, C. J. Quantitation of Metal Content in the Silver-Assisted Growth of Gold Nanorods. *J. Phys. Chem. B* **2006**, *110* (9), 3990–3994. https://doi.org/10.1021/jp0570972.
- (50) Gorelikov, I.; Matsuura, N. Single-Step Coating of Mesoporous Silica on Cetyltrimethyl Ammonium Bromide-Capped Nanoparticles. *Nano Lett.* **2008**, *8* (1), 369–373. https://doi.org/10.1021/nl0727415.
- (51) Khlebtsov, B. N.; Khlebtsov, N. G. On the Measurement of Gold Nanoparticle Sizes by the Dynamic Light Scattering Method. *Colloid J.* **2011**, *73* (1), 118–127. https://doi.org/10.1134/S1061933X11010078.
- (52) Rodríguez-Fernández, J.; Pérez–Juste, J.; Liz–Marzán, L. M.; Lang, P. R. Dynamic Light Scattering of Short Au Rods with Low Aspect Ratios. *J. Phys. Chem. C* **2007**, *111* (13), 5020–5025. https://doi.org/10.1021/jp067049x.
- (53) Monem, A. S.; Elbialy, N.; Mohamed, N. Mesoporous Silica Coated Gold Nanorods Loaded Doxorubicin for Combined Chemo–Photothermal Therapy. *Int. J. Pharm.* **2014**, *470* (1–2), 1–7. https://doi.org/10.1016/j.ijpharm.2014.04.067.
- (54) Carey, V. P. *Liquid-Vapor Phase-Change Phenomena*; Taylor and Francis: Boca Raton, 2020.
- (55) Fisher, J. C. The Fracture of Liquids. *J. Appl. Phys.* **1948**, *19* (11), 1062–1067. https://doi.org/10.1063/1.1698012.
- (56) Visscher, M.; Lajoinie, G.; Blazejewski, E.; Veldhuis, G.; Versluis, M. Laser-Activated Microparticles for Multimodal Imaging: Ultrasound and Photoacoustics. *Phys. Med. Biol.* **2019**, *64* (3), 034001. https://doi.org/10.1088/1361-6560/aaf4a2.
- (57) Arnal, B.; Perez, C.; Wei, C.-W.; Xia, J.; Lombardo, M.; Pelivanov, I.; Matula, T. J.; Pozzo, L. D.; O'Donnell, M. Sono-Photoacoustic Imaging of Gold Nanoemulsions: Part I. Exposure Thresholds. *Photoacoustics* **2015**, *3* (1), 3–10. https://doi.org/10.1016/j.pacs.2014.12.001.

- (58) Schrof, S.; Pang, G.; Buchmann, J.; Laufer, J. Exploiting Nonlinear Photoacoustic Signal Generation in Gold Nanospheres for Selective Detection in Serial 3D PA Tomography. *J. Imaging* **2018**, *4* (12), 146. https://doi.org/10.3390/jimaging4120146.
- (59) Simandoux, O.; Prost, A.; Gateau, J.; Bossy, E. Influence of Nanoscale Temperature Rises on Photoacoustic Generation: Discrimination between Optical Absorbers Based on Thermal Nonlinearity at High Frequency. *Photoacoustics* **2015**, *3* (1), 20–25. https://doi.org/10.1016/j.pacs.2014.12.002.
- (60) Liu, J.; Stace-Naughton, A.; Jiang, X.; Brinker, C. J. Porous Nanoparticle Supported Lipid Bilayers (Protocells) as Delivery Vehicles. *J. Am. Chem. Soc.* **2009**, *131* (4), 1354–1355. https://doi.org/10.1021/ja808018y.
- (61) Shahbazi, K.; Frey, W.; Chen, Y.-S.; Aglyamov, S.; Emelianov, S. Photoacoustics of Core—Shell Nanospheres Using Comprehensive Modeling and Analytical Solution Approach. *Commun. Phys.* **2019**, *2* (1), 119. https://doi.org/10.1038/s42005-019-0216-7.
- (62) Inzunza-Ibarra, M. A.; Premillieu, E.; Grünsteidl, C.; Piestun, R.; Murray, T. W. Sub-Acoustic Resolution Optical Focusing through Scattering Using Photoacoustic Fluctuation Guided Wavefront Shaping. *Opt. Express* **2020**, *28* (7), 9823. https://doi.org/10.1364/OE.385320.